Microfluidic Device Flow Field Characterization Around Tumor Spheroids with Tunable Necrosis Produced in an Optimized, Off-chip Process

James Baye†, Casey Galvin†, Amy Q. Shen

The Okinawa Institute of Science and Technology Graduate School, 1919-1 Tancha, Onna-son, Kunigami-gun, Okinawa-ken, Japan 904-0495

amy.shen@oist.jp

Abstract

Tumor spheroids are a 3-D, *in* vitro tumor model that holds promise for testing cancer therapies *in vitro* using microfluidic devices. Understanding how to tailor the properties of a tumor spheroid is critical for evaluating a therapy over a broad range of possible indications. We use human cancer colon cells (HCT-116) to produce tumor spheroids with targeted diameters and demonstrate the ability to manipulate the microenvironment of the spheroids. We further investigate the flow field around a tumor spheroid contained in a microfluidic device, and show the effect of that flow field on nanoparticle accumulation on the perimeter of the tumor spheroid.

We demonstrate how to control tumor spheroid growth rates by varying the number of cells initially seeded into microwell growth chambers. Furthermore, the presence of a necrotic core in the spheroids could be controlled by changing the glucose concentration of the incubation medium. This manipulation had no effect on the size of the tumor spheroids or hypoxia in the spheroid core, which has been predicted by a mathematical model in computer simulations of spheroid growth. Control over the presence of a necrotic core while maintaining other physical parameters of the spheroid presents an opportunity to assess the impact of core necrosis on therapy efficacy.

Using micro-particle imaging velocimetry (micro-PIV), we characterize the hydrodynamics and mass transport of nanoparticles in tumor spheroids in a microfluidic device. We observe a geometrical dependence on the flow rate experienced by the tumor spheroid in the device, such that the “front” of the spheroid experiences a higher flow velocity than the “back” of the spheroid. Using fluorescent nanoparticles, we demonstrate a heterogeneous accumulation of nanoparticles at the tumor interface that correlates with the observed flow velocities. The penetration depth of these nanoparticles further into the tumor spheroid is size dependent, consistent with reports in the literature.

Keywords

Tumor spheroids, microfluidics, necrotic core, targeted delivery, micro-PIV

† These authors contributed equally to this article.

1 Introduction

Cancers are among the leading causes of morbidity and mortality worldwide, with approximately 14 million new cases and 8.2 million cancer related deaths in 2012. The number of new cases per year is expected to rise by 70% in the next two decades (Stewart et al. 2014). The failure to translate new discoveries into actual therapies is due to inherent differences in results found between the treatment of tumors in murine and other animal models and actual human tumors (Nichols and Bae 2012). This difference has led to greater motivation to construct *in vitro* models that are alternatives to animal models (Elliott and Yuan 2011; Hirschhaeuser et al. 2010; Ricketts et al. 2014; Theodoraki et al. 2015). Accurate *in vitro* models for cancer therapies must capture the 3-D microenvironment of tumors *in vivo* (Kunz-Schughart et al. 2004; Pampaloni et al. 2007). Key features of the tumor microenvironment include hypoxic and necrotic cores, which have been implicated in drug resistance observed in tumors (Elliott and Yuan 2011; Sutherland 1988). The presence of hypoxia or necrosis in the tumor core results from nutrient gradients induced by reduced mass transport due to the tumor's 3-D structure (Jain 1999; Sutherland 1988). 2-D models, such as cell monolayers, fail to capture these types of phenomena, and thus can skew the efficacy of cancer therapies (Karlsson et al. 2012).

Tumor spheroids are an established 3-D *in vitro* model of tumors that are easy to produce, and can achieve features like hypoxic and necrotic cores at size scales consistent with *in vivo* tumors (Achilli et al. 2012; Costa et al. 2016; Hirschhaeuser et al. 2010; Ivascu and Kubbies 2006; Ravizza et al. 2009; Sutherland 1988; Theodoraki et al. 2015; Wang et al. 2014). Since the spheroid is a 3-D structure, it replicates the limited transport of blood-borne nutrients and solutes experienced *in vivo* by portions of a tumor distant from the vasculature (Albanese et al. 2013a; Albanese et al. 2012; Cabral et al. 2011; Raghavan et al. 2016). Tumor spheroids also offer a convenient platform for construction of mathematical models to describe cell proliferation (Ambrosi and Mollica 2002; Drasdo et al. 2007; Drasdo and Höhme 2005). Tumor spheroids result from the self-assembly of cancer cells due to cell-cell interactions, and several techniques and instruments have been developed to create tumor spheroids (Alessandri et al. 2013; Drewitz et al. 2011; Froehlich et al. 2016; Fu et al. 2014; Karlsson et al. 2012; Mehesz et al. 2011; Ravizza et al. 2009; Santo et al. 2016). While automated systems for spheroid production are an ongoing area of research, there remains a need for straightforward, inexpensive schemes to produce tumor spheroids in order for the general research community to have access to these *in vitro* tumor models. Furthermore, understanding how the properties of tumor spheroids, such as diameter or the presence of a necrotic core, can be manipulated by easily accessible conditions (e.g., initial cell count or nutrient concentration) enables the *in vitro* investigation of tumor treatment therapies over a broader range of tumor conditions.

In addition to preparing accurate *in vitro* models of tumors, it is necessary to replicate the *in vivo* environment surrounding the tumor—specifically, the vasculature system. Error! Reference source not found.**a** depicts a simplified view of a tumor mass embedded in a capillary network (Nichols and Bae 2012; Sutherland 1988). Mass transport from the capillary into the tumor vasculature delivers nutrients that sustain tumor growth, and provides a means for delivering solution-borne therapeutics into the tumor. Microfluidic devices are ideally suited for replicating the scenario shown in Error! Reference source not found.**a**, due to the ability to fabricate devices with channel dimensions similar to the human vasculature system, and good control over the environment inside of the device (Khademhosseini et al. 2006; Whitesides 2006). Error! Reference source not found.**b** shows a schematic of the microfluidic device used in this study, which is based on a recently reported design (Albanese et al. 2013b). The design of the device allows the sequestration of a tumor spheroid with a diameter of around 400 μm in a region of the device suitable for direct observation using microscopy techniques. The flow of solution-borne nutrients and therapeutics occur from left to right, and the

uptake of fluorescent markers or the response of the tumor spheroid to a solution-borne therapeutic can be tracked using standard microscopy techniques.

This article examines two aspects of the use of tumor spheroids. The first aspect considers how to manipulate the properties of the tumor spheroid, in particular the diameter and presence of core necrosis. The first set of experiments in this work develops an optimized protocol for producing tumor spheroids with targeted diameters in commonly available microwell plates. The second set of experiments shows how the nutrient profile of the incubation media used to culture the tumor spheroids affects the microenvironment within the resulting spheroids. In particular, we manipulate the presence of a necrotic core in a tumor spheroid by changing the glucose concentration of the incubation media. These experiments show how the tumor spheroid production process can be optimized to achieve tumor spheroids with tailored properties for researchers who do not have access to automated spheroid growing systems. The results of these experiments further allow us to confirm experimentally an observation made in a computer simulation of tumor spheroid growth (Drasdo and Höhme 2005), which found that glucose concentration affected core necrosis without affecting the growth rate of the tumor spheroids.

The second set of experiments in this article characterize the flow profile around the tumor spheroid in the microfluidic device (shown in Error! Reference source not found.**b**) using microparticle imaging velocimetry (micro-PIV). Our results reveal a heterogeneous fluid velocity profile impinging on the spheroid, which correlates with a heterogeneous distribution of nanoparticle accumulation at the spheroid perimeter.

2 Materials and Methods

2.1 Media Preparation

2.1.1 Cell culture medium

DMEM with phenol red containing 4.5 g/L glucose (high glucose) or 1 g/L glucose (low glucose), 110 mg/mL sodium pyruvate, 584 mg/L L-glutamine and 3.7 g/L $NaHCO_3$ (Life Technologies cat. nos. 11995065 &11885-084), supplemented with 100 U/ml penicillin, 100 mg/ml streptomycin (Life Technologies, cat. no. 15070063), and 10 v% Fetal Bovine Serum (Life Technologies, cat. no. 12483020) was used as a standard medium for cell and spheroid culturing.

2.1.2 Imaging medium

An aqueous solution of 2 g/L bovine serum albumin, 125mM NaCl, 5.7mM KCl, 2.5mM CaCl2, 1.2mM MgCl2, 10mM HEPES at pH 7.4 was used as a standard imaging medium for microscopy analysis of spheroids (Albanese et al. 2013a).

2.2 Spheroid Culturing and Analysis

2.2.1 Cancer cell culture

Colon HCT116, Lung A549 and Glioblastoma U87MG cancer cells were obtained by generous donation from Cell Signal Unit at OIST. Cells were seeded in typical plastic bottom flasks (Corning, cat. no. CLS430641), maintained in cell culture medium (see above) and incubated under typical cell culture conditions at 37°C, 5% CO_2 in humidified incubators. Routine passaging of colon cancer cells (HCT116) was performed every 3-4 days by detaching cells with Accutase (Nacalai cat. no. 12679-54) and reseeding at 1:10 (3 days) or 1:25 (4 days) dilutions.

2.2.2 Spheroid culture plate preparation

To prevent cell attachment either agarose or poly(2-hydroxyethyl methacrylate) (PHEMA) were used to coat 96-well plates. Agarose coating was conducted as previously reported (Friedrich et al. 2009). Briefly, coating was performed 2 hours before cell seeding by adding 50 µL of 15 g/L agarose in cell culture medium to flat-bottomed wells. The 15 g/L agarose solution preparation procedure typically consisted in adding agarose powder (Sigma cat. No. A9539) to culture medium, autoclaving 20 min at 120°C to dissolve the powder and directly transferring and maintaining the solution in a 70°C water bath during dispensing to avoid the solution hardening. After dispensing, agarose hardened in wells in seconds to minutes, forming a concave bed for cells. PHEMA coating was performed in round-bottom wells by dispensing 50 µL 20 g/L PHEMA in 95 v% EtOH and air drying overnight at room temperature, producing a thin homogeneous film coating. The 20 g/L PHEMA solution was prepared by dissolving PHEMA powder (Sigma cat. no. P3938) in a 95 v% EtOH aqueous solution overnight in a tightly sealed beaker, heated at 80°C with agitation.

2.2.3 Cancer cell spheroid seeding

Colon cancer cells grown as a monolayer were detached with Accutase and 200 µL of the cell solution containing 500-2000 cells were distributed into single wells of 96 well plates pre-coated with either agarose or PHEMA (refer to Spheroid culture plate preparation above). Plates were then centrifuged 5 min at 1000 rpm using a swinging bucket Eppendorf Centrifuge (Eppendorf AG) and incubated under typical cell culture conditions at 37°C, 5% CO_2 in humidified incubators. By day 3 of culture, cells formed into compact spheroids and were analyzed.

2.2.4 Spheroid size and quality analysis

Spheroid size was analyzed in ImageJ by fitting an ellipse to the spheroid images captured by phase contrast microscopy (Olympus SZX7 upright microscope). Spheroid diameter was then defined as the quadratic mean of the small and large ellipse diameters. Spheroids were defined of good quality if they showed good signs of compactness and no clear irregularities in their circularity. Some examples of both properly formed and poorly formed spheroids are shown in **Figure S1**.

2.3 Cell Staining Protocols

2.3.1 Histological staining

Spheroids were fixed in 4 v% paraformaldehyde (PFA) in Phosphate Buffer Saline (PBS) for 1 hour at room temperature. The PFA solution was prepared fresh two hours prior to fixing by dissolving PFA powder (Sigma P6148) in PBS (Nacalai cat. no. 14249-24) heated at 80°C with thorough agitation. The fixed spheroids were then individually embedded in OCT Compound (Sakura Finetek, cat. no. 4583), placed in cryomolds (Sakura Finetek, cat. no. 4728) and snap frozen at the interface of liquid nitrogen on floating aluminium foil boats. Frozen samples were stored at -80°C and then transferred to a cryostat (Leica CM3050s) for sectioning where 10 µm sections of the spheroid were cut, retrieved on MAS-coated glass slides (Matsunami, cat. no. S9441) and air dried overnight. Finally, histological staining was performed following the protocol previously described (Ellis), with the slight difference that the eosin was prepared in aqueous form and that the mounting medium used was aqueous-based, thus avoiding any dehydration steps.

2.3.2 Hypoxia immunostaining

Spheroids were cryosectioned in the same way as for histological staining with the slight difference that spheroids were incubated with pimonidazole prior to fixation and sectioned at a 5 µm thickness. Briefly, a 4 mM pimonidazole in PBS stock was prepared from pimonidazole powder (Hypoxyprobe, cat. no. HP2-100) and added to spheroids at a final concentration of 200 µM, followed by a 1 hour incubation in a humidified incubator at 37°C, 5% CO_2. Typical immunostaining, as previously described

(Aguilera and Brekken 2014), was then performed against pimonidazole to reveal hypoxic regions by the use of mouse FITC-conjugated IgG1 monoclonal antibodies (clone 4.3.11.3) (Hypoxyprobe, cat. no. HP2-100). Following immunostaining, sample nuclei were counterstained for 15 min with 0.5 µg/mL Hoechst (Sigma, cat. no. H6024). Finally, slides were mounted and a coverslip was placed on top of the slide, and observed by fluorescence microscopy (Zeiss LSM510 inverted microscope).

2.3.3 Spheroid live-dead cell imaging

Calcein-AM (Nacalai, cat. no. 06735-81) and Propidium Iodide (Nacalai, cat. no. 29037-76) were used for live cell and dead cell staining respectively. Calcein-AM and Propidium Iodide were added to spheroid culture wells at final concentrations of 10 µg/mL and 20 µM respectively and incubated for 4 hours at 37°C, 5% CO_2 in humidified incubators. Spheroids were then transferred in imaging medium (refer to REAGENT SETUP) and seeded in glass slide chambers (Nunc, cat. no. 177402) pre-coated with 200 µL of 100 g/L Bovine Serum Albumin (Sigma, cat. no. A2153) for 1 hour. Images were captured by confocal microscopy (Zeiss LSM510 confocal microscope).

2.4 Microfluidic Device Fabrication and Characterization of Spheroid Containing Devices

2.4.1 Microfluidic device preparation

Microfluidic devices were fabricated by molding and crosslinking PDMS (Dow Corning, Sylgard 184) on an epoxy resin master previously produced by soft lithography in clean room conditions. The cured PDMS mold was irreversibly bound to a glass coverslip petri dish (ibidi, cat. no. 81158) using oxygen plasma (Harrick, PDC-001) followed by heating at 100°C for 1 hour. Care was taken to punch a 2 mm diameter hole through the PDMS at the device inlet to form a well for spheroid seeding, whereas the outlet was connected to Tygon tubing (BD Intrimedic, cat. no. 427406) for later connection to a syringe pump system (negative pressure-driven flow). The microfluidic device was designed with a channel height of 380 µm in order to slightly compress the 400 µm spheroids in order to ensure adequate immobilization for imaging. The channel entrance is 600 µm wide and widens further to 1,200 µm at the imaging chamber to ensure the laminar flow profile surrounding the spheroids before arriving at the dam wall to minimize physical damage.

2.4.2 Microfluidic device flow field characterization by Micro-Particle Image Velocimetry (micro-PIV)

The microfluidic device was precoated for 1 hour with 100 g/L Bovine Serum Albumin (Sigma, cat. no. A2153) followed by 3 washes of imaging medium (see Reagent Setup section). Spheroids were then loaded with gentle, pressure driven flow of imaging medium. The device was then mounted on the micro-PIV stage and a dilute solution of 3.2 µm fluorescent polystyrene beads in a 25 v% glycerol and imaging medium solution was flowed through the system. Glycerol was used to avoid particle sedimentation, and did not visually affect spheroid morphology. At 25 v%, the solution viscosity increased to twice the viscosity of water. The micro-PIV imaging system comprises a 1280 x 800 pixel, CMOS camera (Phantom Micro M310, Vision Research Inc., NJ), an inverted microscope (Nikon Eclipse TE 2000) and a dual-pulsed Nd:YLF laser (Terra PIV, Continuum Inc., CA) emitting at 527 nm. A 4x, NA = 0.13 numerical aperture objective attached to the microscope is used to focus on the midplane of the tumor spheroid contained in the microfluidic device viewing chamber. Illumination of the focused area by the laser causes the fluorescent microparticles to emit a longer wavelength than the excitation wavelength. The reflected laser light is filtered out, so that the camera detects only the fluorescent microparticles. The camera records pair of images with a pre-defined time step between each image so that the microparticles translate approximately 4 pixels between each image. The image pairs were

analyzed with the standard cross-correlation PIV algorithm (TSI Insight 4G software), and the results further analyzed in Tecplot Focus software (Tecplot Inc., WA).

2.4.3 Nanoparticle penetration and accumulation assay

Rhodamine-B conjugated polystyrene beads (Nanocs cat. nos. PS20-RB, PS50-RB) with 20nm and 50 nm diameters were characterized by dynamic light scattering (Malvern Zetasizer Nano ZS) prior to the experiment, in typical experimental conditions (0.0634% (wt/vol) in imaging medium at 37°C). Nanoparticle concentration was determined by approaching the clinical administration values found in literature (Yanagie et al. 2014). Device preparation followed the same protocol as that for the micro-PIV, specifically coating with Bovine Serum Albumin then washing with imaging medium. Next, the device was mounted on a cell culture stage (37°C, 5% CO2). Flow rate was controlled using a syringe pump (cetoni GmbH neMESYS low pressure syringe pump), with flow being driven by an empty syringe applying negative pressure to the outlet and medium containing nanoparticles replenishing the inlet well at an equal rate. Nanoparticle accumulation images were taken using a 63x oil immersion objective on a ZEISS LSM780 confocal microscope. Images were taken at three different heights z = {50;75;100 µm} of the spheroid. Fluorescence distribution was analyzed with a Matlab program developed in-house that localized the spheroid edge and measured mean fluorescence at various depths throughout the spheroid. Fluorescence values were then averaged on whole cell layers (10 µm depth radial contractions) and normalized to the fluorescence of the surrounding media to give accumulation values per cell layer.

3 Results and Discussion

When cultured on a flat, cell-adhesive surface, cells typically form into a monolayer cell sheet where the predominant interaction is the cell-substrate interaction (Pampaloni et al. 2007). Conversely, seeding of cells on a non-adhesive surface (e.g., agarose) leads to the predominant formation of cell-cell and cell-matrix interactions. Moreover, by bringing these cells into close contact – typically by seeding them in non-adhesive concave shaped wells – the cells will be much more likely to form 3-D tumor spheroids (Achilli et al. 2012; Pampaloni et al. 2007; Sutherland 1988), as illustrated in Error! Reference source not found.**a**.

Three cell lines were first tested for spheroid formation: lung cancer cells (A549), brain glioblastoma cancer cells (U87MG), and colon cancer cells (HCT-116). Our results show that only HCT-116 cells formed clear spheroids (*cf*. **Figure S1**), consistent with other successful reports of HCT-116 spheroid culturing (Karlsson et al. 2012; Ravizza et al. 2009). For this reason, we selected this cell line for the current study.

3.1 Controlled Tumor Spheroid Fabrication and Growth Rates

In order to facilitate our experiments using tumor spheroids in a microfluidic device, we sought to develop a production scheme that would allow us to produce spheroids of a target diameter on a given day. We conceived of a strategy to seed a variable number of initial cells for spheroid growth, and looked at the time required for each condition to reach target spheroid sizes. We hypothesized that the incubation time required for a spheroid to reach a target size would decrease with an increasing number of initial cells loaded. In this way, we could achieve a staggered growth schedule of tumor spheroids.

In order to assess the optimal cell seeding and incubation time for achieving tumor spheroids of a given size by the strategy described above, spheroids were grown in microwells coated with agarose and seeded with an initial number of cells per well ranging from 250 to 6000. **Figure 2b** plots the spheroid diameter obtained from optical microscopy as a function of incubation time from days 4 to

6 for the different quantities of initially seeded cells. The diameters observed for an initial seeding of 500 cells/well are consistent with HCT-116 spheroids grown using an automated hanging drop method (Drewitz et al. 2011), confirming the suitability of our culture setup. The solid lines are linear fits of the data sets, and illustrate the linear dependence of spheroid size on incubation time for different initial quantities of seeded cells during the observation period (Drasdo and Höhme 2005; Drewitz et al. 2011; Freyer and Sutherland 1985). Prior to day 4, there is a lag period in growth, followed by an exponential increase in the spheroid diameter as cells begin to aggregate into a spheroid. From day 4 onward, the increase in spheroid diameter is presumably due to cell division (Drasdo and Höhme 2005).

From the linear fits plotted in Error! Reference source not found.**b**, we can estimate the time necessary to reach our target spheroid size. Error! Reference source not found.**c** plots the incubation time to achieve spheroids with target diameters of 200, 400 and 600 μm. The error bars are determined from errors associated with the linear fitting in Error! Reference source not found.**b**. Using these data, we were able to achieve a supply of fresh tumor spheroids with the target diameter each day to facilitate our experiments using the tumor spheroids in microfluidic devices. One interesting feature of these data is the different slope of the linear fit, which is a measure of spheroid growth rate over the fitted date range. These slopes are plotted in **Figure S2** as a function of initial number of seeded cells. There is a clear reduction in growth rate as the initial number of seeded cells increase. While our current study did not allow us to precisely elucidate the mechanism underlying this trend, we surmise that a reduction in quantity of nutrients per cell with increasing initial cell count (Drasdo and Höhme 2005) and stress generated on cells due to confinement in the spheroid (Ambrosi and Mollica 2002) are primary, coupled factors.

In conducting the experiments described in Error! Reference source not found., we observed that not all of the spheroids formed into the expected spherical shape, and instead produced many smaller spheroids or misshaped samples. Examples of poorly formed spheroids are shown in **Figure S1** in the Supporting Information. We hypothesized that the curvature of the agarose coating was not sufficient to promote the settling of the tumor cells at the bottom of the well. Furthermore, the curvature of the agarose surface varies from well to well, which affects the consistency of the spheroid growth process. If the curvature of the coated well increased, the cells would settle more quickly to the bottom of the well and would have a higher probability of forming a single spheroid due to proximity. This concept is illustrated in **Figure 3a**. To test this hypothesis, we used an alternative coating material—poly2-hydroxymethyl methacrylate) (PHEMA)—to coat curved microwells (Ivascu and Kubbies 2006). The PHEMA coating produced a much thinner film than the agarose deposited into flat-bottom wells. Since the spheroid ultimately forms on the geometry created by the surface coating, a thinner coating better preserves the geometry of the microwell. As a result, the PHEMA-coated curved microwells presented the desired curvature to compare against the relatively flat coating produced by the agarose. Due to the way the agarose gel is deposited into the microwell and solidifies, it cannot be formed into thin films like PHEMA, thus masking the curvature of the microwell.

The results of spheroid formation in both well types under identical conditions of 4.5 g/L of glucose (i.e., high glucose as defined below) are plotted in **Figure 3b**. The bars indicate the number of properly formed and poorly formed spheroids for the agarose-coated wells (green) and PHEMA-coated wells (blue) as determined by visual inspection. The agarose data show that after 3 days of incubation, no spheroids had properly formed. With increasing incubation time, the agarose coated wells start to produce spheroids, and the fraction of these spheroids that are properly formed increases with incubation time. In contrast, the PHEMA-coated wells produced properly formed spheroids by day 3, and in a quantity comparable to longer incubation times. We conclude that the greater curvature achieved by the thinner, more uniform coating in the PHEMA-coated wells enhanced the production

of properly formed spheroids by promoting the initial aggregation of the cancer cells in each microwell into a single spheroid.

3.2 Manipulation of the Tumor Microenvironment

With a protocol for producing properly formed spheroids established, we now turn our attention to the microenvironment in the tumor spheroid. Hypoxic cells have been reported to be more resistant to certain drugs (Brown 2007) and necrotic cell regions could impede drug penetration (Shannon et al. 2003). The presence of hypoxic cells and secondary necrosis is a direct function of nutrient supply. It has been shown that under typical culture conditions, cell constructs of sizes larger than 200 µm contain hypoxic cells, and that necrotic cores exist in constructs of sizes greater than 500 µm due to the presence of chemical gradients at such size scales (Hirschhaeuser et al. 2010). We targeted tumor spheroids with a diameter of 400 µm in order to determine whether necrosis is present at this spheroid size. This size is also consistent with the dimensions of a recently reported microfluidic device for studying uptake of nanoparticles and small molecules (Albanese et al. 2013b).

Since microenvironmental conditions like hypoxic and necrotic cores are implicated in therapy resistance in tumors (Cabral et al. 2011), it is advantageous if the presence of such features can be manipulated easily in an *in vitro* tumor model. Since hypoxic and necrotic cores result from gradients of oxygen and nutrients (e.g., glucose), respectively, varying the concentration of oxygen and nutrients affects the formation and extent of these features (Drasdo and Höhme 2005; Freyer and Sutherland 1986; Jain 1999). In manipulating the presence of hypoxic and necrotic cores, it is important that the targeted tumor spheroid size can be attained for further experimentation. We tested whether the presence of a necrotic core in the HCT-116 spheroids could be manipulated by simply changing the glucose concentration in the incubation media from 4.5 g/L to 1.0 g/L, and if this had an effect on growth rates of the spheroids.

As a starting point, histological staining and immunostaining were performed to probe the density of the spheroids and presence of a hypoxic core. Error! Reference source not found.Error! Reference source not found. shows characteristic images for both staining techniques for tumor spheroids produced under high glucose (4.5 g/L) and low glucose (1.0 g/L) conditions in agarose-coated microwells. The results from histological staining (left column) show that whether cultured in low or high glucose concentrations, spheroids formed nicely packed cellular structures (density 80-90%). Furthermore, for similarly sized spheroids grown under identical conditions, immunostaining shows that the spheroids contain hypoxic cells at an average depth of 100 µm. Since the level of oxygen in the incubation environment remained constant for both glucose levels, it is expected that the presence of hypoxia should be similar for both spheroids.

To determine whether the variation in glucose level had the desired effect of manipulating the presence of necrotic cores, spheroids were assayed for the presence of live and dead cell content, with characteristic results shown in Error! Reference source not found. for spheroid incubation times of 5 days and 7 days at high and low glucose concentration. The assay stains live cells green and dead cells red. For the high glucose content images (top row), there is a perimeter of living cells on the spheroid, while dead cells appear scattered sparsely throughout the spheroid. In contrast, the low glucose images display a concentrated core of dead cells in the spheroid, indicating the formation of a necrotic core. For both glucose concentrations, there is a large region of apparently quiescent cells between the viable rim and core of the spheroids, consistent with computer simulation results (Drasdo

and Höhme 2005). The cited computer simulation model starts from a single cell capable of dividing and incorporates mass transport and mechanical forces into the growing spheroid. The model reproduced successfully tumor spheroid growth data from prior literature reports (Freyer and Sutherland 1986), and the growth data presented in Error! Reference source not found. exhibits a linear trend as predicted by the computer simulation model.

For samples prepared in high and low glucose concentrations, analysis of spheroid diameters plotted in **Figure S3** revealed no significant difference for a wide range of initial cell seeding values. The fact that the presence of the necrotic core depends on the glucose concentration, while the size of the spheroids does not is consistent with computer simulations of tumor spheroids (Drasdo and Höhme 2005). Furthermore, the necrotic core appears to grow in diameter and density with increasing incubation time. Although the necrotic cores shown at day 7 are clearly of two different diameters, our current data do not allow us to quantify how precisely the size of the core can be controlled. Nonetheless, the results of this assay show that the presence of a necrotic core depends on glucose concentration, and its presence can be manipulated by changing glucose concentration and incubation time without affecting overall spheroid size.

To summarize our results of producing an *in vitro* tumor model, we have successfully prepared human colon cancer tumor spheroids. In doing so, we demonstrated the ability to tailor the size of the spheroids by varying the initial number of seeded cells and incubation time. The spheroids produced using our protocol resulted in densely packed samples that exhibited hypoxic cores. The presence of necrotic cores in these samples could be manipulated by simply changing the glucose concentration in the incubation medium, which had no significant effect on the spheroid growth rate, as predicted by computer simulations (Drasdo and Höhme 2005). With a suitable tumor model created, we will now focus on the characterization of the flow field around a tumor spheroid contained in a microfluidic system for *in vitro* tumor therapy assessment.

3.3 Micro-PIV Characterization of Microfluidic Device with Tumor Spheroid

We fabricated a microfluidic device based on a previously reported design (Albanese et al. 2013b) that mimics the flow of a branching capillary on a tumor mass (*cf*. **Figure 1b**). In order for a tumor vasculature mimic to be physiologically relevant, it should effectively reproduce the flow velocities present in *in vivo* vasculature. Fluid velocities were thus measured in the device by using microparticle image velocimetry (micro-PIV), which tracks the movement of microparticles to characterize the flow field of the fluid carrying the microparticles (*cf*. Materials and Methods). **Figure 6a** and **6b** show a tumor spheroid contained within the observation chamber of the microfluidic device in a fluid containing fluorescent microparticles using brightfield and fluorescence microscopy, respectively. Micro-PIV uses a series of images similar to that shown in **Figure 6b** to determine the velocity and direction of the fluid flow. Using flow rates of 25 nL/s and 125 nL/s resulted in the velocity fields shown in **Figure 6c** and **6d**, respectively, which are plotted using the same color scale. The measured velocities were found to be in the physiological range of mice capillaries (75-675 µm/s) (Albanese et al. 2013b).

An additional system parameter to consider is the shear stress on the tumor spheroid, which should be below 0.1 Pa to avoid affect cellular behavior (Dimmeler et al. 2015). Shear stress can be estimated by considering both cross sections on the left and right of the seeded spheroid to be cylinders. Shear stress was determined by applying the formula describing shear stress along a cylinder wall:

$$\tau = \mu \frac{4Q}{\pi r^3}$$

Where Q is the volumetric flow rate of the fluid, μ is the fluid dynamic viscosity and r is the radius of the cylinder used to model the space between the tumor spheroid and the wall. The maximum shear stress on the tumor mass was estimated to be 0.042, which is below the 0.1 Pa minimum threshold known to affect cell behavior (Dimmeler et al. 2015)

In order to assess the profile of the flow velocity around the spheroid, the velocities from **Figure 6c** and **6d** were taken along lines cut at either x = 1.6 mm or y = 0.0 mm. These velocities are plotted in **Figure 7a** and **7b**, respectively for flow rates of 25 nL/s (black squares) and 125 nL/s (red circles). The profiles are similar in shape for both flow rates, with different magnitudes of the flow velocities. As seen in **Figure 7a**, the velocity on the sides of the spheroid parallel with the flow direction are quite similar, consistent with the symmetry of the microfluidic system. In contrast, the velocities on the sides of the spheroid perpendicular to the flow are clearly different, with the "front" of the spheroid experiencing a flow rate ~ 3x greater than that of the "back" of the spheroid.

With the heterogeneous velocity results of **Figure 7** in mind, we assessed the accumulation and penetration of fluorescent polystyrene nanoparticles with diameters of either 20 nm or 50 nm in the tumor spheroid. Nanoparticle size was measured by dynamic light scattering under observation conditions (identical imaging temperature and identical imaging buffer) in order to check nanoparticle size and detect any particle aggregation. No particle aggregation was observed over a 60 minute timescale (data not shown) and the size range measured by dynamic light scattering was consistent with that expected (*cf*. **Figure S1**).

The effect of the asymmetric velocity profile observed in **Figure 7b** was measured by integrating the intensity of the fluorescence over a 15^{o} arc on the front center and back center of spheroids exposed to 20 and 50 nm particles at 125 nL/s (*cf*. **Figure S2**). The ratio of the front side intensity to back side intensity is displayed in **Table 1**, with both the 20 nm and 50 nm particles showing a higher intensity in the front than the back (i.e., ratio is greater than unity). While our data can only provide a preliminary conclusion, if this *in vitro* result mimics *in vivo* performance, this geometrical effect in particle uptake highlights an additional challenge in effectively targeting tumors with nanoparticles.

Table 1 Relative fluorescence intensity of the front side and back side of tumor spheroids.

Particle Diameter	**Intensity Ratio of Front Side to Back Side**
20 nm	1.33
50 nm	1.19

We next analyzed the penetration of 20 nm nanoparticles into the tumor spheroids over a period of 60 minutes, the results of which are plotted in **Figure 8a**. The fluorescence intensity within the spheroid was averaged over 10 μm thick layers down to a total depth of 50 μm. A thickness of 10 μm was chosen because it is the mean diameter of the cells forming the spheroids as assessed by microscopy images. The data sets are grouped in terms of "cell layers" (i.e., 10 μm increments). For all depths, there is an increase in intensity with exposure time, followed by a plateau after ≈45 minutes. While the first 20 μm of depth in the spheroid has essentially the same fluorescence intensity, and thus concentration of nanoparticles, subsequent depths exhibit markedly lower fluorescence. Since the fluorescence intensity has plateaued by 60 minutes, this time point was chosen to analyze the effect of flow rate and particle diameter on nanoparticle penetration.

The results in Error! Reference source not found.**b** plot fluorescence intensity for each 10 µm thick slab extending into the spheroid exposed to 20 and 50 nm particles at 125 nL/s flow rate (black squares and red circles, respectively), and 20 nm particles with no flow (open square). There is a clear increase in fluorescence intensity in the first 20 µm of depth for the 20 nm particles under flow compared to the 50 nm particles. However, this difference rapidly decreases beyond 20 µm of depth. Without flow, the 20 nm particles show a similar profile to that observed for the 50 nm particles with flow. While this overlap is probably coincidental, it does illustrate the significant effect convection has on nanoparticle uptake.

These results illustrate an overall poor penetration capacity of the polystyrene nanoparticles into our *in vitro* tumor mimic, and is characteristics of the observation that nanoparticles of the size used in this study cannot penetrate the interstitial space between tumor cells (Cabral et al. 2011; Huang et al. 2012; Huo et al. 2013; Perrault et al. 2009; Wong et al. 2011). This result is in spite of the fact that the exterior of the spheroid appears to saturate with nanoparticles, as seen in Error! Reference source not found.**a**. Even in this ideal simulation, where a continuous flow of nanoparticles was applied without flushing, the smallest size nanoparticle (20nm) barely managed to penetrate 50 µm in distance into the tumor mass. This distance is still far from the 100 µm distance required to reach hypoxic cells, let alone the 200-250 µm threshold where central necrosis is found. With intercapillary distance in tumor tissue ranging (in certain cases) to several hundred microns, these results underline the need to design highly penetrating nanoparticles by taking advantage of particle size and surface chemistry, or using a different delivery strategy.

4 Conclusion

We have successfully prepared human colon cancer tumor spheroids from HCT-116 cells. In doing so, we demonstrated the ability to tailor the size of the spheroids by varying the initial number of seeded cells and incubation time. The spheroids produced using our protocol resulted in densely packed samples that exhibited hypoxic cores. The presence of necrotic cores in these samples could be manipulated by simply changing the glucose concentration in the incubation medium, which had no significant effect on the spheroid growth rate, both verified by our experiments and predicted by a computer simulation model (Drasdo and Höhme 2005). We further examined the flow profile around a tumor spheroid contained in a recently described microfluidic device using micro-PIV. This flow profile correlated with a heterogeneous accumulation of fluorescent polystyrene nanoparticles at the perimeter of the tumor spheroid. The further penetration of these nanoparticles into the tumor spheroid exhibited a dependence on nanoparticle size and the flow rate of the surrounding media, consistent with observation for other nanoparticle systems. Going forward, this platform will allow evaluation of therapeutic nanoparticles and other tumor therapies in lab settings, while covering a broad range of tumor microenvironments to illustrate the effect microenvironment has on tumor therapies.

5 Acknowledgements

We gratefully acknowledge support from the OIST Graduate University with subsidy funding from the Cabinet Office, Government of Japan. We also thank the Yamamoto unit at OIST for providing cells and helpful discussions.

6 References

T.-M. Achilli, J. Meyer, and J. R. Morgan, Expert Opin. Biol. Ther. **12**, 1347 (2012).
K. Y. Aguilera and R. A. Brekken, **4**, 1 (2014).

A. Albanese, A. K. Lam, E. A. Sykes, J. V. Rocheleau, and W. C. W. Chan, Nat. Commun. **4**, 2718 (2013a).
A. Albanese, A. K. Lam, E. a Sykes, J. V Rocheleau, and W. C. W. Chan, Nat. Commun. **4**, 2718 (2013b).
A. Albanese, P. S. Tang, and W. C. W. Chan, Annu. Rev. Biomed. Eng. **14**, 1 (2012).
K. Alessandri, B. R. Sarangi, V. V. Gurchenkov, B. Sinha, T. R. Kießling, L. Fetler, F. Rico, S. Scheuring, C. Lamaze, A. Simon, S. Geraldo, D. Vignjević, H. Doméjean, L. Rolland, A. Funfak, J. Bibette, N. Bremond, and P. Nassoy, Proc. Natl. Acad. Sci. **110**, 14843 (2013).
D. Ambrosi and F. Mollica, Int. J. Eng. Sci. **40**, 1297 (2002).
J. M. Brown, Methods Enzymol. **435**, 297 (2007).
H. Cabral, Y. Matsumoto, K. Mizuno, Q. Chen, M. Murakami, M. Kimura, Y. Terada, M. R. Kano, K. Miyazono, M. Uesaka, N. Nishiyama, and K. Kataoka, Nat. Nanotechnol. **6**, 815 (2011).
E. C. Costa, A. F. Moreira, D. de Melo-Diogo, V. M. Gaspar, M. P. Carvalho, and I. J. Correia, Biotechnol. Adv. **34**, 1427 (2016).
S. Dimmeler, J. Haendeler, V. Rippmann, M. Nehls, and A. M. Zeiher, FEBS Lett. **399**, 71 (2015).
D. Drasdo, S. Hoehme, and M. Block, J. Stat. Phys. **128**, 287 (2007).
D. Drasdo and S. Höhme, Phys. Biol. **2**, 133 (2005).
M. Drewitz, M. Helbling, N. Fried, M. Bieri, W. Moritz, J. Lichtenberg, and J. M. Kelm, Biotechnol. J. **6**, 1488 (2011).
N. T. Elliott and F. Yuan, J. Pharm. Sci. **100**, 59 (2011).
R. Ellis, (n.d.).
J. P. Freyer and R. M. Sutherland, J. Cell. Physiol. **124**, 516 (1985).
J. P. Freyer and R. M. Sutherland, Cancer Res. **46**, 3504 (1986).
J. Friedrich, C. Seidel, R. Ebner, and L. A. Kunz-Schughart, Nat. Protoc. **4**, 309 (2009).
K. Froehlich, J.-D. Haeger, J. Heger, J. Pastuschek, S. M. Photini, Y. Yan, A. Lupp, C. Pfarrer, R. Mrowka, E. Schleußner, U. R. Markert, and A. Schmidt, J. Mammary Gland Biol. Neoplasia 1 (2016).
C.-Y. Fu, S.-Y. Tseng, S.-M. Yang, L. Hsu, C.-H. Liu, and H.-Y. Chang, Biofabrication **6**, 015009 (2014).
F. Hirschhaeuser, H. Menne, C. Dittfeld, J. West, W. Mueller-Klieser, and L. A. Kunz-Schughart, J. Biotechnol. **148**, 3 (2010).
K. Huang, H. Ma, J. Liu, S. Huo, A. Kumar, T. Wei, X. Zhang, S. Jin, Y. Gan, P. C. Wang, S. He, X. Zhang, and X.-J. Liang, ACS Nano **6**, 4483 (2012).
S. Huo, H. Ma, K. Huang, J. Liu, T. Wei, S. Jin, J. Zhang, S. He, and X.-J. Liang, Cancer Res. **73**, 319 (2013).
A. Ivascu and M. Kubbies, J. Biomol. Screen. **11**, 922 (2006).
R. K. Jain, Annu. Rev. Biomed. Eng. **1**, 241 (1999).
H. Karlsson, M. Fryknäs, R. Larsson, and P. Nygren, Exp. Cell Res. **318**, 1577 (2012).
A. Khademhosseini, R. Langer, J. Borenstein, and J. P. Vacanti, Proc. Natl. Acad. Sci. U. S. A. **103**, 2480 (2006).
L. A. Kunz-Schughart, J. P. Freyer, F. Hofstaedter, and R. Ebner, J. Biomol. Screen. **9**, 273 (2004).
A. N. Mehesz, J. Brown, Z. Hajdu, W. Beaver, J. V. L. da Silva, R. P. Visconti, R. R. Markwald, and V. Mironov, Biofabrication **3**, 025002 (2011).
J. W. Nichols and Y. H. Bae, Nano Today **7**, 606 (2012).
F. Pampaloni, E. G. Reynaud, and E. H. K. Stelzer, Nat. Rev. Mol. Cell Biol. **8**, 839 (2007).
S. D. Perrault, C. Walkey, T. Jennings, H. C. Fischer, and W. C. W. Chan, Nano Lett. **9**, 1909 (2009).
S. Raghavan, P. Mehta, E. N. Horst, M. R. Ward, K. R. Rowley, and G. Mehta, Oncotarget **7**, 16948 (2016).
R. Ravizza, R. Molteni, M. B. Gariboldi, E. Marras, G. Perletti, and E. Monti, Eur. J. Cancer **45**, 890 (2009).
K. P. M. Ricketts, U. Cheema, A. Nyga, A. Castoldi, C. Guazzoni, T. Magdeldin, M. Emberton, A. P. Gibson, G. J. Royle, and M. Loizidou, Small **10**, 3954 (2014).

V. E. Santo, M. F. Estrada, S. P. Rebelo, S. Abreu, I. Silva, C. Pinto, S. C. Veloso, A. T. Serra, E. Boghaert, P. M. Alves, and C. Brito, J. Biotechnol. **221**, 118 (2016).
A. M. Shannon, D. J. Bouchier-Hayes, C. M. Condron, and D. Toomey, Cancer Treat. Rev. **29**, 297 (2003).
B. W. Stewart, C. Wild, International Agency for Research on Cancer, and World Health Organization, editors , *World Cancer Report 2014* (International Agency for Research on Cancer, Lyon, France, 2014).
R. M. Sutherland, Science **240**, 177 (1988).
M. Theodoraki, C. J. Rezende, O. Chantarasriwong, A. Corben, E. Theodorakis, and M. Alpaugh, Oncotarget **6**, 21255 (2015).
C. Wang, Z. Tang, Y. Zhao, R. Yao, L. Li, and W. Sun, Biofabrication **6**, 022001 (2014).
G. M. Whitesides, Nature **442**, 368 (2006).
C. Wong, T. Stylianopoulos, J. Cui, J. Martin, V. P. Chauhan, W. Jiang, Z. Popović, R. K. Jain, M. G. Bawendi, and D. Fukumura, Proc. Natl. Acad. Sci. **108**, 2426 (2011).
H. Yanagie, S. Higashi, K. Seguchi, I. Ikushima, M. Fujihara, Y. Nonaka, K. Oyama, S. Maruyama, R. Hatae, M. Suzuki, S. Masunaga, T. Kinashi, Y. Sakurai, H. Tanaka, N. Kondo, M. Narabayashi, T. Kajiyama, A. Maruhashi, K. Ono, J. Nakajima, M. Ono, H. Takahashi, and M. Eriguchi, Appl. Radiat. Isot. **88**, 32 (2014).

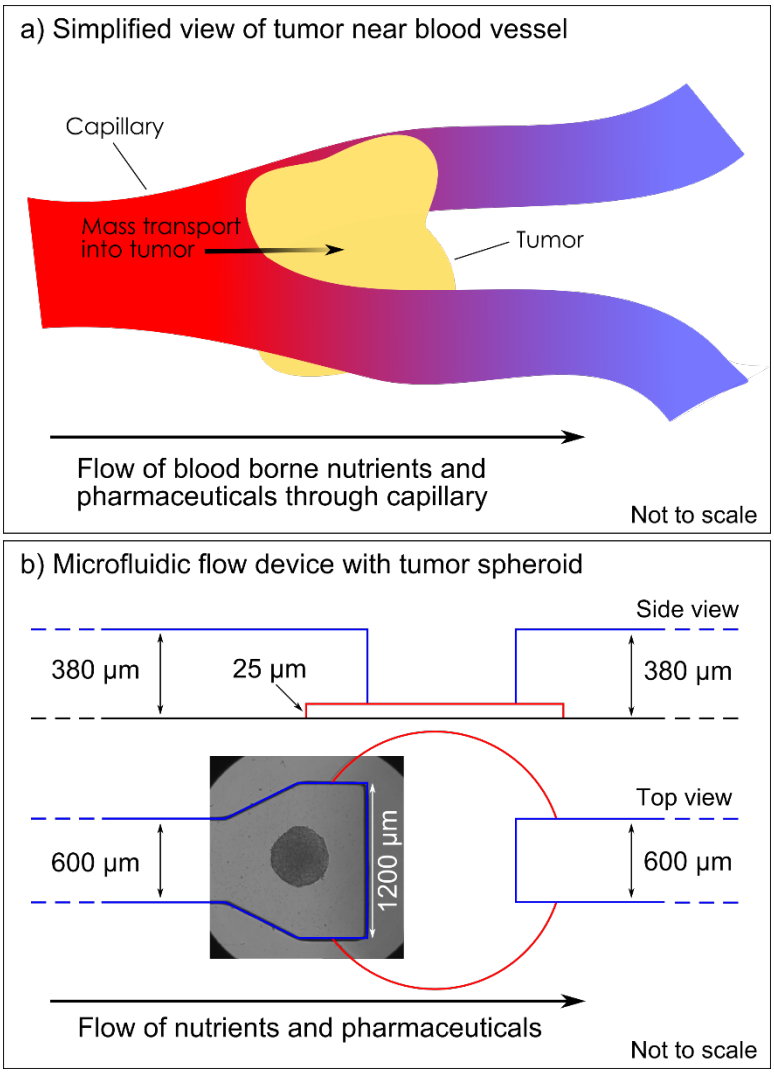

Fig. 1 (a) Tumors can receive blood borne nutrients through the vasculature system. This same mode of delivery can be used to expose *in vivo* tumors to pharmaceutical agents. (b) The schematic shows a microfluidic device designed to replicate the *in vivo* blood vessel flow. The channels outlined in blue had thickness of 380 µm and widths of 600 µm. These dimensions were chosen to mimic dimensions within the human body. The inlet channel expands to a width of 1200 µm to create an imaging chamber to observe spheroid responses to materials carried within the flow channel (e.g., nanoparticles or pharmaceutical agents). The red, circular region is a dam 25 µm in thickness to enable sequestration of the spheroid in the imaging chamber. An optical microscopy image of a tumor spheroid contained within the imaging chamber of the microfluidic device is superimposed over the device schematic.

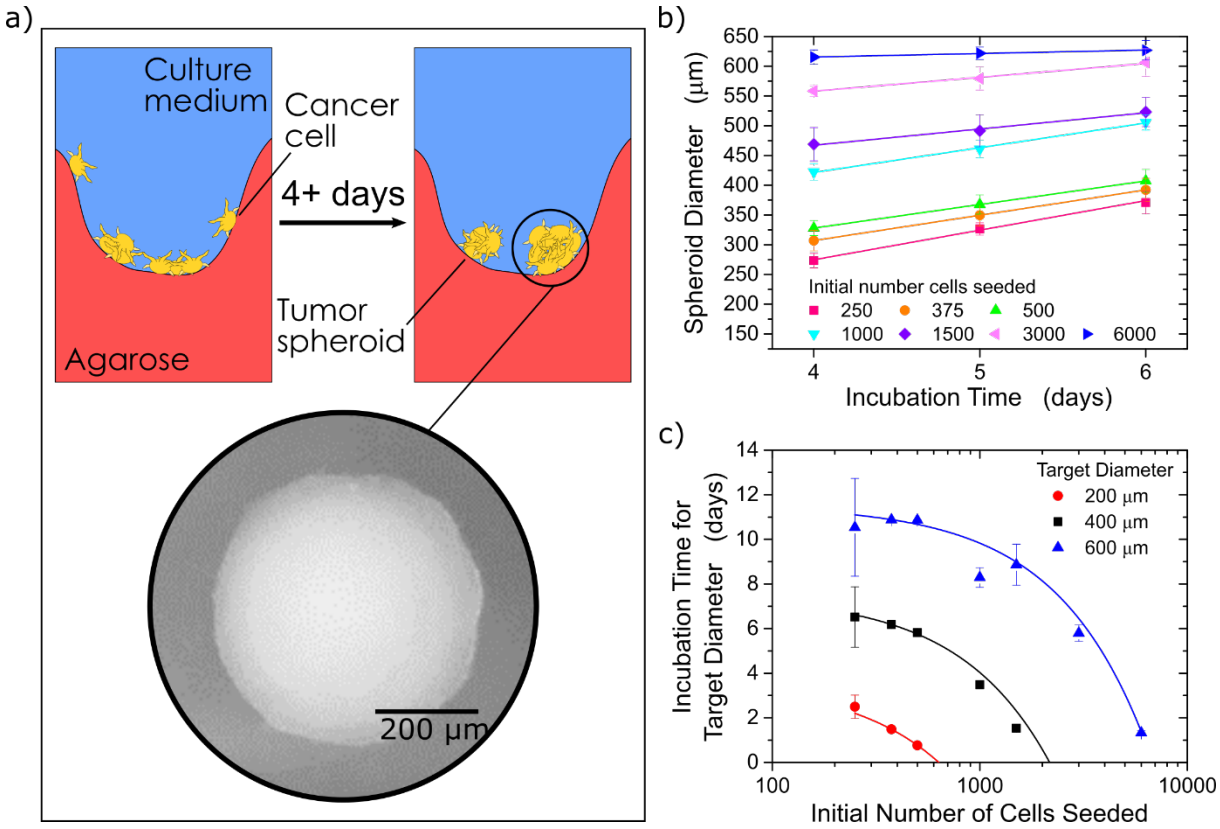

Fig. 2 (a) Schematic showing the method of producing tumor spheroids by incubating cancer cells in agarose-coated cylindrical, flat-bottom wells. At sufficiently long incubation times, the cancer cells spontaneously form into tumor spheroids. The inset shows a brightfield microscopy image of a properly shaped (i.e., spherical) tumor spheroid. (b) Tumor spheroid diameter plotted as a function of incubation time for different initial numbers of seeded cells. The solid lines are linear fits to the data. (c) Required incubation time for a given number of cells seeded initially into a microwell for target tumor spheroid diameters of 200 μm (red circles), 400 μm (black squares) and 600 μm (blue triangles). The solid lines are linear fits of each data set plotted on the log scale. The fits had R^2 values of 0.99 (red), 0.97 (black) and 0.99 (blue). Images not drawn to scale.

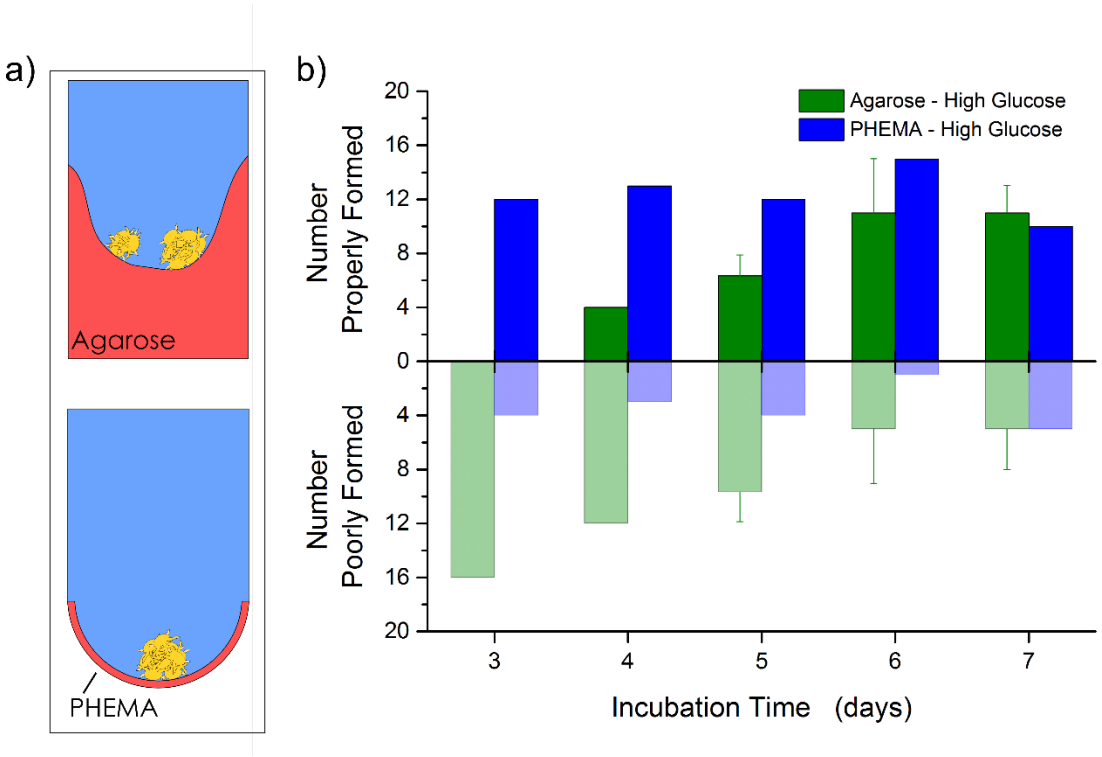

Fig. 3 (a) Possible end results for culturing cancer cells in an agarose-coated well (top) and PHEMA-coated round bottom well (bottom). The thin film of PHEMA preserves the shape of the round bottom well, resulting in sedimentation of cells at the bottom of the well and rapid formation of properly shaped, spherical spheroids. (b) Comparison of spheroid shape for agarose-coated wells (green) and PHEMA coated wells (blue). Agarose-coated wells initially form spheroids that are poorly shaped, which then grow into well formed spheroids. In contrast, PHEMA-coated wells rapidly form properly formed spheroids. The error bars correspond to the standard deviation of two separate experiments.

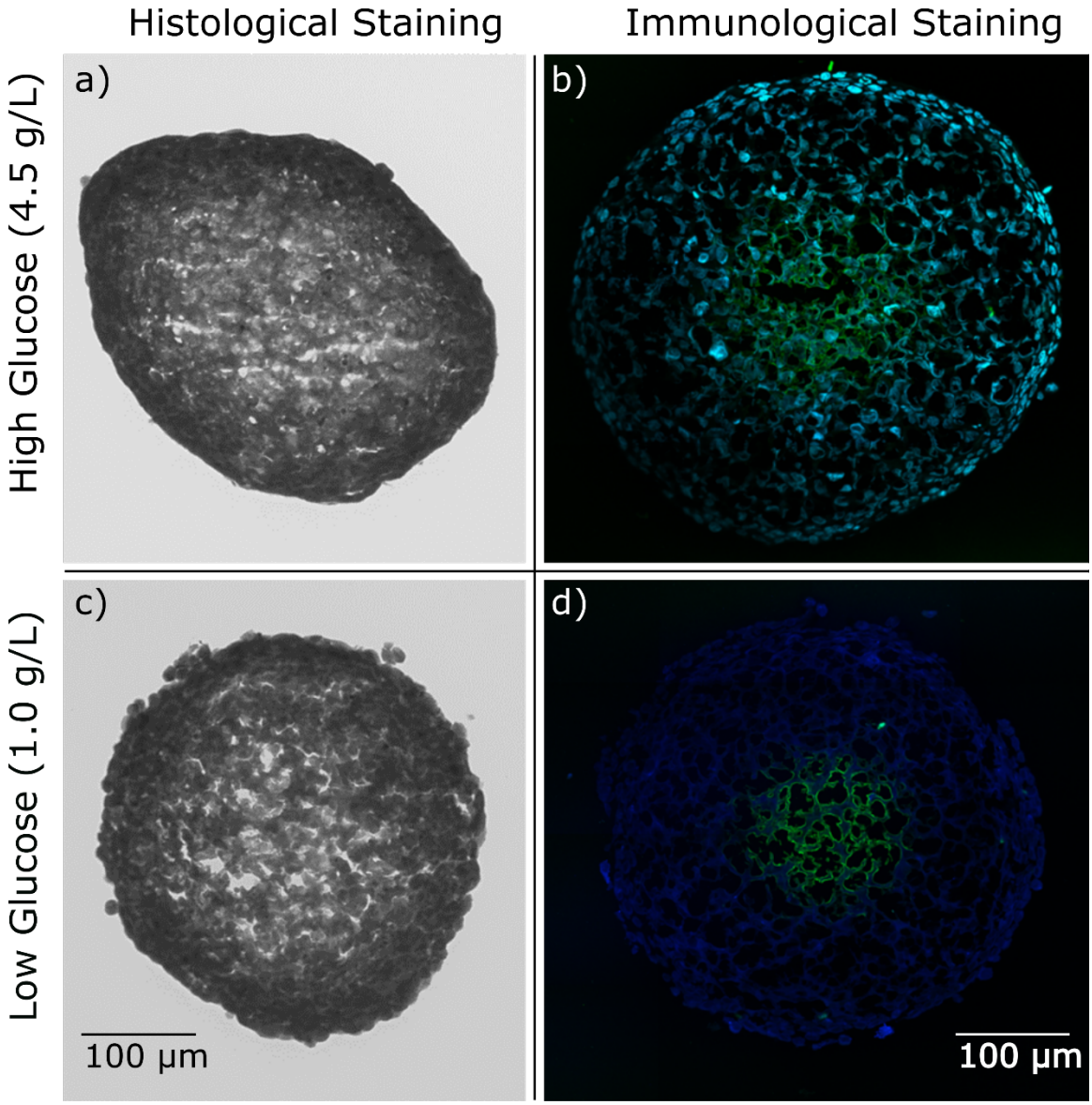

Fig. 4 Spheroids cultured in high (a, b) and low (c, d) glucose concentration conditions were analyzed by histological staining (a, c) to reveal cell packing and by immunostaining to reveal hypoxic regions (b ,d). Immunostaining enables simultaneous visualization of cell nuclei (blue) and hypoxic regions (green). All spheroids were harvested after 5 days of culture except for the high glucose immunostained sample which was cultured for 7 days.

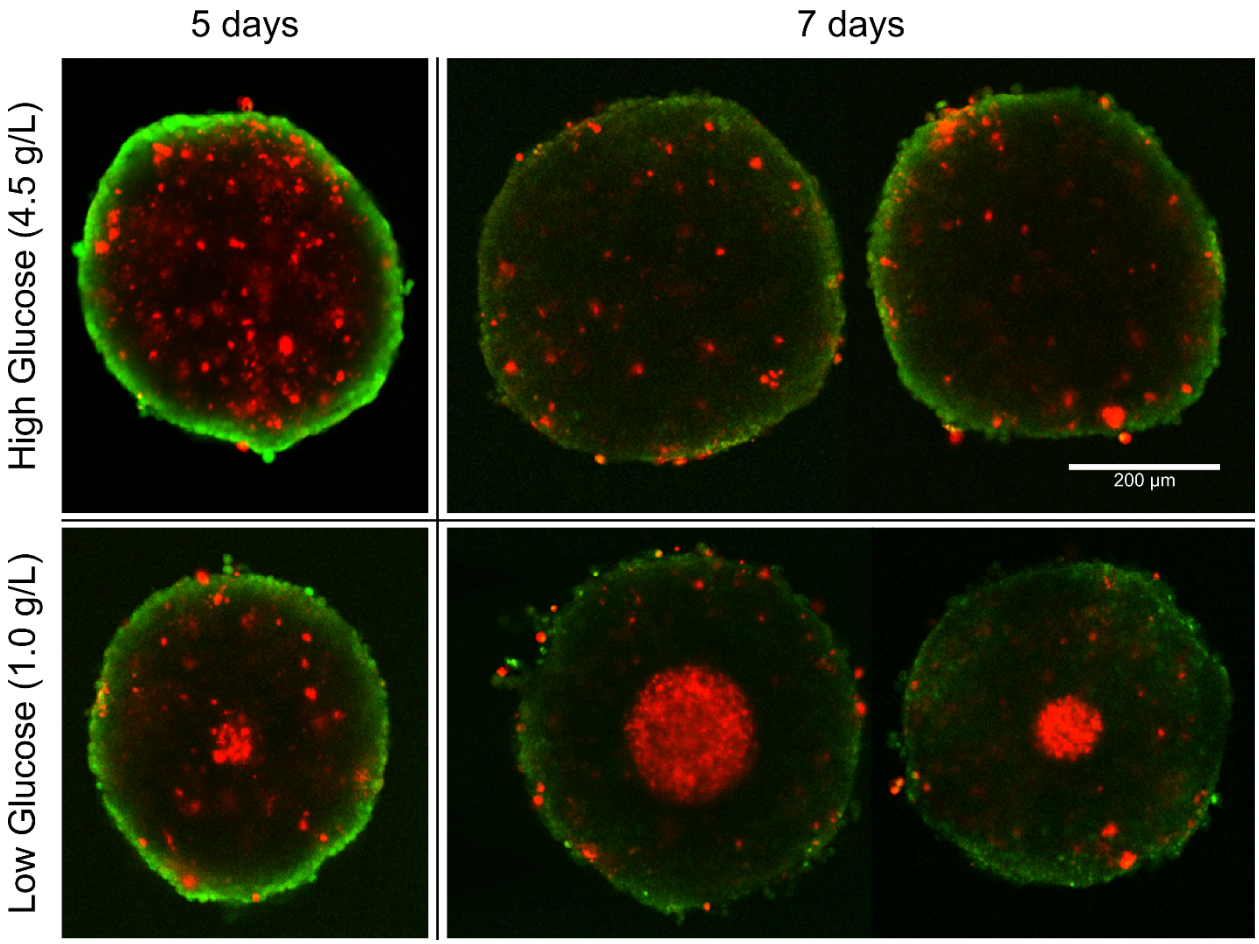

Fig. 5 Midplane captures of proliferating cells (green) and dead cells (red) in spheroids cultured for 5 days (left) and 7 days (right) at high glucose (top) and low glucose (bottom) conditions. The scale bar corresponds to length scales for both high and low glucose images.

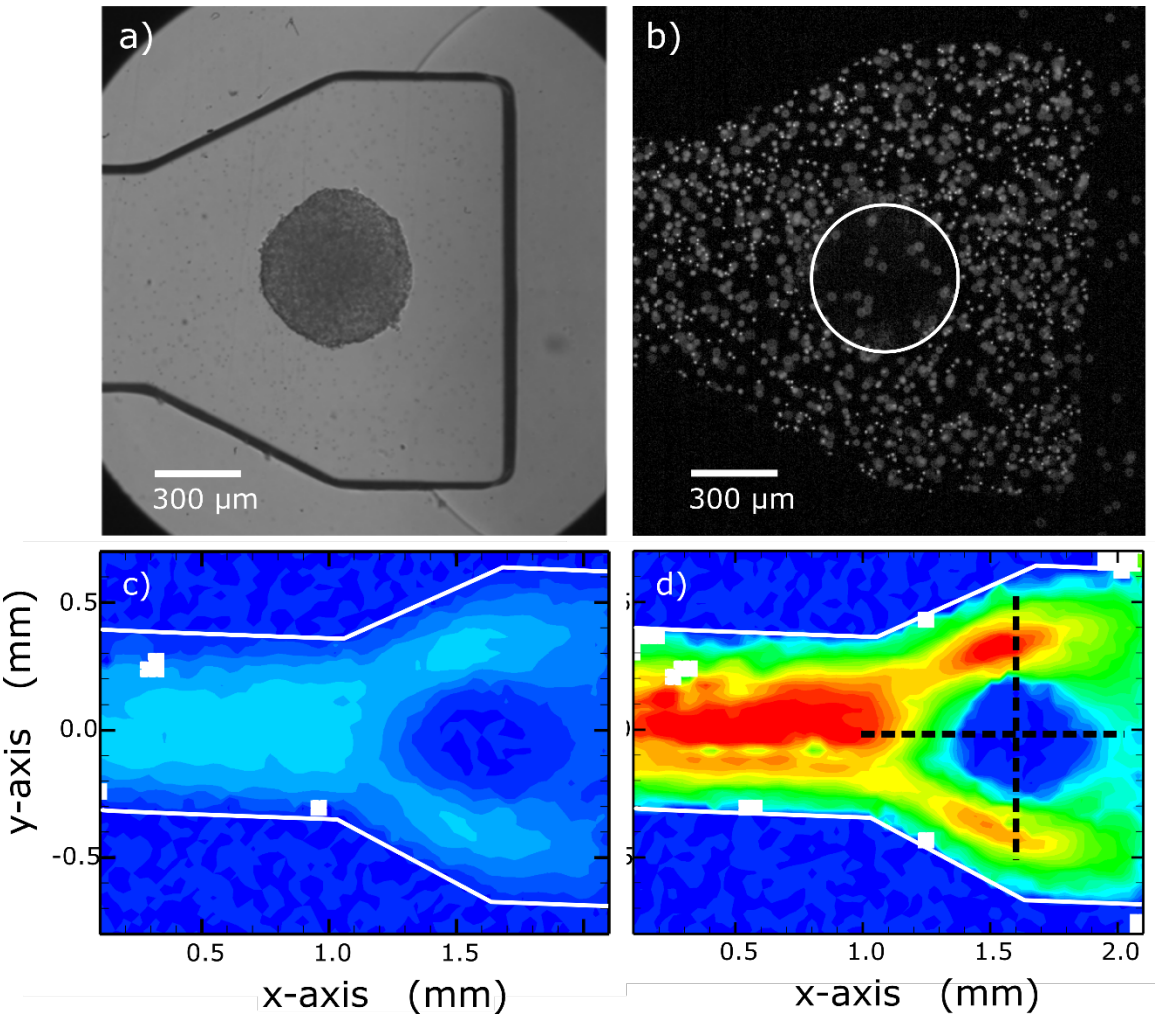

Fig. 6 (**a**) Phase contrast image of spheroid sequestered in the device imaging chamber. (**b**) Raw data collected from the micro-PIV showing fluorescent microparticles and spheroid (outlined by the white line) in the device imaging chamber. (**c**, **d**) Fluid velocity inside device in the presence of a cancer cell spheroid determined by the micro-PIV for flow rates of 25 nl/s (**c**) and 125 nl/s (**d**). The dashed black line in panel d corresponds to the data shown in **Figure 7**.

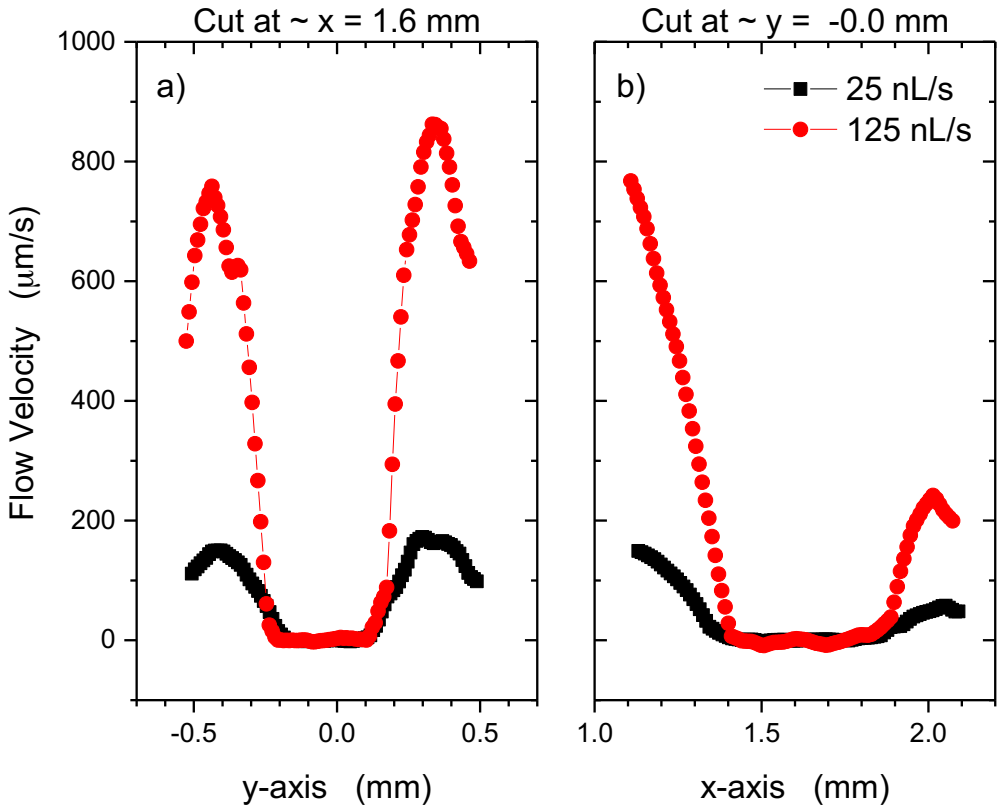

Fig. 7 Line cuts taken from the data in Fig. **6**d for volumetric flow rates of 25 nL/s (black) and 125 nL/s (red). (a) Cut made along the x-axis at ~1.6 mm (i.e., middle of the spheroid) showing the velocity profile along the y-axis for both volumetric flow rates. (b) Cut made along the y-axis at ~-0.5 mm (i.e., middle of the spheroid) showing the velocity profile along the x-axis for both volumetric flow rates. While the y-axis velocity profile shows a symmetrical profile about the spheroid for both flow rates, the x-axis velocity profile shows a higher velocity at the front of the spheroid compared to the back of the spheroid relative to the direction of flow.

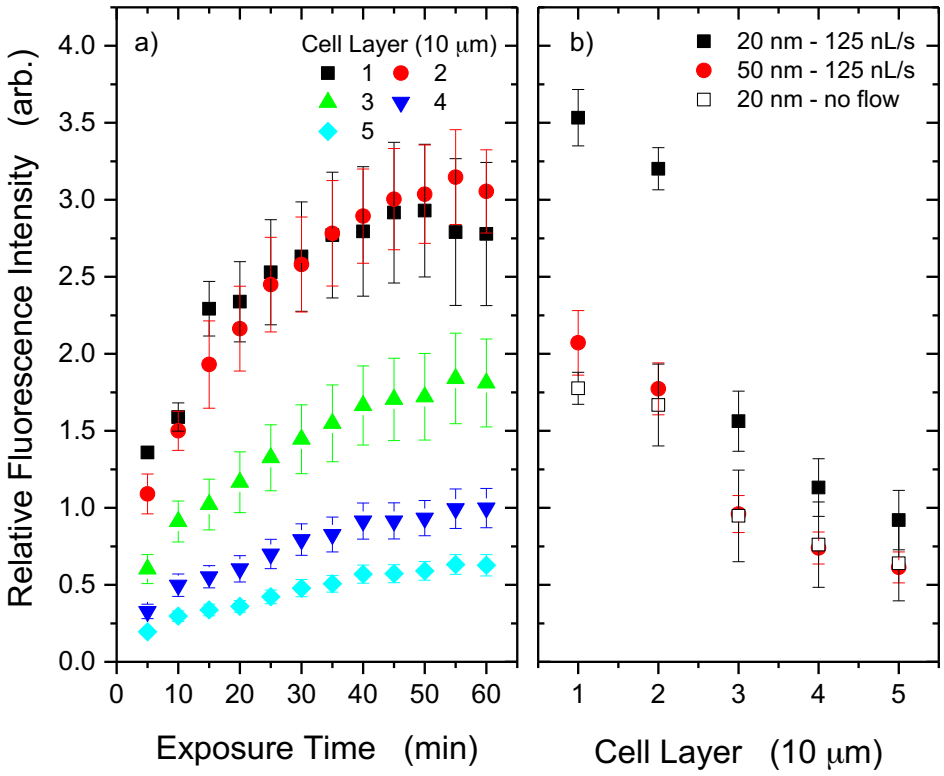

Fig. 8 (a) Fluorescence intensity of 20 nm nanoparticles for different depths in a tumor spheroid as a function of exposure time. (b) Fluorescence intensity in tumor spheroids exposed to fluorescent nanoparticles with diameters of 20 nm (black, filled squares) or 50 nm (red, filled circles) at 125 nL/s, or 20 nm with no flow (black, open squares). Cell layer was calculated by assuming the average cell is 10 μm in diameter, thus the first cell layer represents the first 10 μm from the perimeter of the spheroid inward.